ACS Photonics

pubs.acs.org/journal/apchd5

Article

PT-Symmetric Absorber-Laser Enables Electromagnetic Sensors with Unprecedented Sensitivity

Mohamed Farhat, Minye Yang, Zhilu Ye, and Pai-Yen Chen*

Cite This: https://dx.doi.org/10.1021/acsphotonics.0c00514

Read Online

ACCESS | Metrics & More | Article Recommendations | Supporting Information

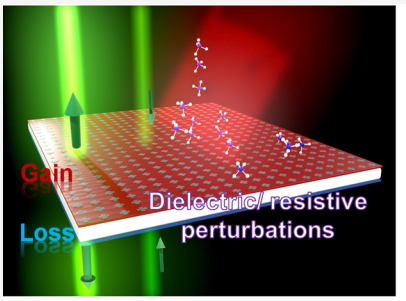

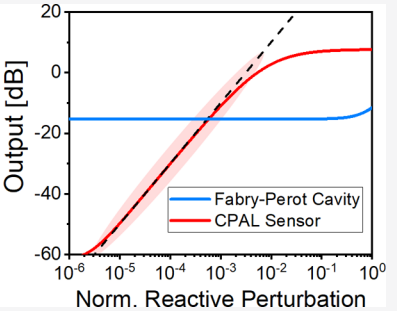

ABSTRACT: Achieving extraordinarily high sensitivity is a long-sought goal in the development of novel and more capable electromagnetic sensors. We present here how a coherent perfect absorber-laser (CPAL) enabled by parity-time (PT) symmetry breaking may be exploited to build ultrasensitive monochromatic electromagnetic sensors that use radio waves, microwaves, terahertz radiations, or light. We argue the possibility of using such CPAL sensors to detect extremely small-scale perturbations of admittance or refractive index caused by, for example, low-density gas molecules and microscopic properties, as they may drastically vary the system's output intensity from very low (coherent absorption) to high (lasing). We derive the physical bounds on CPAL sensors, showing that their sensitivity and resolvability may go well beyond traditional electromagnetic sensors, such as sensors based on Fabry−Perot cavities.

KEYWORDS: *parity-time symmetry, laser oscillators, coherent perfect absorbers, electromagnetic sensors, RF and microwave sensing, optical sensing*

Unusual points in the spectra of non-Hermitian Maxwellian systems, such as exceptional points (EPs),[1−13] have recently attracted notable attention in diverse fields ranging from optics, photonics,[1−13] acoustics,[14,15] and radio frequency electronics.[16−25] These isolated points of the spectrum are generally missed in a generic situation and may require special engineering of the system, such as parity-time (PT)-symmetric ones with separated, judiciously balanced gain and loss. To date, EPs existing in PT-symmetric non-Hermitian systems have opened up many remarkable new applications, including unidirectional invisibility,[5,26] negative refraction, and subdiffraction imaging,[27,28] optical isolators, and circulators,[29,30] as well as high-sensitivity optical and electronic sensing systems enabled by complex frequency splitting in the proximity of EPs.[20−23,31−34] In addition, a PT-symmetric system displays a self-dual spectral singularity, at which the lasing state and the CPA state (viewed as time-reversed lasing) may coexist at a given wavelength, so-called CPAL point.[13,41−46] In general, a CPA represents a dark medium that fully absorbs incoming radiations, whereas a laser is a radically different concept intended to produce the zero-linewidth, coherent electromagnetic radiation propagating outward an active medium. For linear two-port networks obeying PT-symmetry (see Figure 1a), at the CPAL point, eigenvalues of the scattering matrix **S** become zero and infinity, which are associated with the CPA and lasing states, respectively;[13,41] these two states may be switched by adjusting the complex amplitude ratio between two incoming waves. Since scattering coefficients may diverge significantly at this self-dual spectral singularity, PT-symmetric CPAL optical systems have been proposed to build the next-generation soliton switches, logic devices, and single-mode lasing cavities.[13,41−46]

Motived by these recent findings, we propose here the extension of the PT-symmetric CPA-laser to make monochromatic single-wavelength electromagnetic sensors with unprecedented sensitivity, resulting from dramatically modulated scattering properties associated with CPAL actions. As schematically shown in Figure 1b, this sensing system may be

Received: March 31, 2020
Published: July 7, 2020

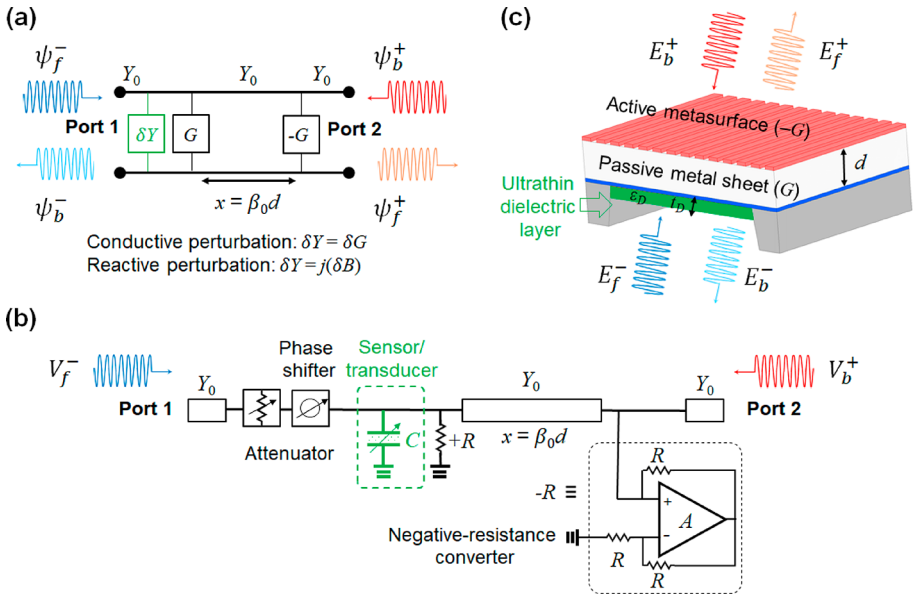

Figure 1. (a) Equivalent transmission-line model for the generalized PT-symmetric sensing system and its practical realization in the (b) RF and microwave region (e.g., with electronic circuits consisting of a lumped resistor and a negative-resistance converter) and (c) optical region (e.g., with a pair of active and passive metasurfaces). In this two-port network, two parallel lumped conductances $G = \gamma Y_0$ and $-G = -\gamma Y_0$ are separated by a portion of transmission line of characteristic admittance Y_0 and electrical length x. The system is perturbed by a variable admittance δY, which may be a reactive contribution $[\delta Y = j(\delta B)]$ or a conductive one $(\delta Y = \delta G)$.

readily implemented in the low-frequency, RF, and microwave regime by exploiting electronic circuits,[15−25] transmission lines,[19] or metasurfaces,[26−28,46,47] of which gain and loss are produced by resistors and active lumped elements (e.g., negative resistance converter[15,20]) and perturbation in impedance of variable elements (e.g., microtransducers with variable capacitance[20] or chemiresistors with variable conductance[21]) may cause dramatic changes in scattering coefficients. In the optical realm, PT-symmetric CPAL systems can be realized using microring resonators,[31,32] fibers,[9−12] or simply a pair of suitably separated active and passive metasurfaces shown in Figure 1c. For optical sensing based on metasurface platforms, admittance perturbations may be caused by deposition of a thin dielectric or conductive layer (e.g., gases, molecules, or aqueous solutions) on the metasurface.

The above-mentioned systems (Figure 1b,c), although working in different spectra and implemented with different techniques, may share a similar two-port transmission-line network (TLN) model shown in Figure 1a, of which lumped conductance (G) and negative conductance $(-G)$ are separated by an electrical length $x = \pi/2 + \delta x$. In an ideal electromagnetic sensing platform, the measured output coefficient must be capable of responding to an infinitesimal change in the local admittance δY; namely, the slope of the output function $\Theta(\delta Y)$ should be as large as possible. As detailed next, if the aforementioned PT-symmetric sensing systems are locked at the CPAL point, the measured scattering response is very sensitive to δY existing in the admittance-variable component. We should also note that such a single-frequency sensing paradigm based upon the CPAL effect is vastly different from those EP-based sensors,[20−23,31,32,47,48] which usually exploit the eigenvalue bifurcation effect to enhance the resonance shift with respect to the external disturbance. Comparing both techniques, the monochromatic sensing scheme proposed here does not require any sophisticated wavelength synthesizers or wideband amplifying devices, thus offering potentially more stable operation and lower implementation cost. Moreover, EP-based sensors, which detect resonant peak shifts in the spectral domain, have been reported to be rather vulnerable to inevitable background noises,[35−40] such as the phase and flicker noises, as well as the modal interference occurring in higher-order EP-based systems. On the contrary, the phase and flicker noises are insignificant in the proposed CPAL-based sensing system because it simply detects power levels of scattered monochromatic waves at a fixed operating frequency.

CONCEPT OF CPAL ACTION IN PT-SYMMETRIC ELECTROMAGNETIC SYSTEMS

Figure 1a features the generalized PT-symmetric electromagnetic system with an admittance distribution: $Y(x') = -G\delta(x') + G\delta(x' - d)$, where $\delta(\cdot)$ is the Dirac delta function. In RF and microwave circuits (Figure 1b), the conductances, G and $-G$, are sourced from a passive resistor and an active negative-resistance converter, respectively, and these two lumped elements are separated by a portion of transmission line with characteristic admittance Y_0 and length $x = \beta_0 d$, where β_0 is the propagation constant in the transmission line of length d. In a similar vein, PT-symmetric systems may also be realized using a pair of metasurfaces with positive and negative surface conductances, separated by a distance d in vacuum or dielectric medium (Figure 1c). Optical media with a deep-subwavelength thickness may be described by a lumped admittance, with a net gain or loss depending on the imaginary part of the dielectric constant.[49] In this sense, an active optical metasurface may be built using a thin slab or sheet of gain medium, such as an optically pumped, patterned two-dimensional (2D) material.[46,47,49−51]

To analyze the scattering from the PT-symmetric system in Figure 1a, the electric field (or ac voltage) on left (−) and right (+) sides $\psi^{\pm} = \psi_f^{\pm} e^{-i\beta x} + \psi_b^{\pm} e^{i\beta x}$ are decomposed into forward-

https://dx.doi.org/10.1021/acsphotonics.0c00514
ACS Photonics XXXX, XXX, XXX−XXX

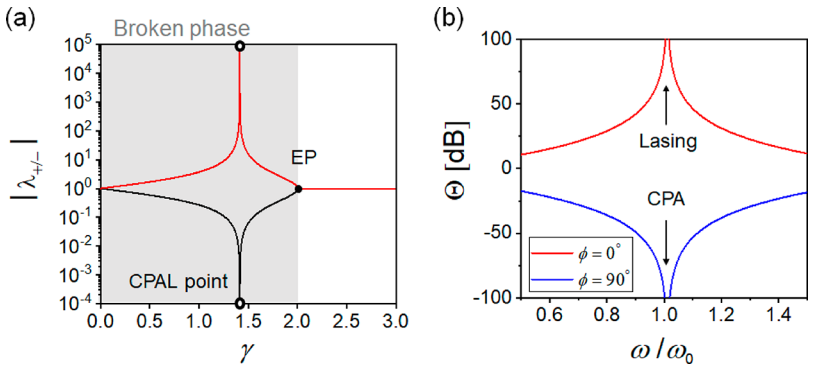

Figure 2. (a) Evolution of eigenvalues as a function of γ for the generalized PT system in Figure 1a; here, $\delta x = 10^{-2}$ and $\delta Y = 0$. The system can be divided into the exact PT-symmetry phase (white) and the broken PT-symmetry (gray) phase, with a discontinuous phase transition at the exceptional point ($\gamma = 2$). In the broken phase, the two eigenvalues approach infinity (lasing state) and zero (CPA state) at the CPAL point ($\gamma = \sqrt{2}$). (b) Output coefficient vs the normalized frequency for the PT system in (a), with $\gamma = \sqrt{2}$ and $d = 0.2475\lambda_0$ (which leads to $\delta x = 10^{-2} \times (\pi/2)$ at the design frequency). We note that the system can be switched between the CPA and lasing modes by adjusting the phase offset ϕ ($\alpha = |M_{21}|e^{-i\phi}$).

and backward-propagating waves, where amplitudes, $\psi_f^{\pm}$ and $\psi_b^{\pm}$, are related by a 2 × 2 transfer matrix $\mathbf{M}$ as: $(\psi_f^+, \psi_b^+)^T = \mathbf{M}(\psi_f^-, \psi_b^-)^T$. In addition, input and output, $|\psi_{in}\rangle = (\psi_f^-, \psi_b^+)^T$ and $|\psi_{out}\rangle = (\psi_f^+, \psi_b^-)^T$ are related by the scattering matrix as $|\psi^{out}\rangle = \mathbf{S}|\psi_{in}\rangle$, where $\mathbf{S} = \begin{pmatrix} t_- & r^+ \\ r^- & t \end{pmatrix}$, and the transmission ($t$) and reflection ($r$) coefficients for left (−) and right (+) incidences can be expressed in terms of transfer matrix elements: $r^- = -M_{21}/M_{22}$, $r^+ = M_{12}/M_{22}$ and $t^+ = t^- = t = 1/M_{22}$.[41] The validity of PT-symmetry imposes a conservation relation: $\mathbf{S}^*(\omega) = \mathrm{PT}\mathbf{S}(\omega)\mathrm{PT} = \mathbf{S}^{-1}(\omega)$,[13] where the parity operator $P \equiv \sigma_1$, the time-reversal operator $T \equiv \sigma_1 K$, σ_1 is the Pauli matrix, and K is the complex conjugation operator. Here, we define a dimensionless gain-loss parameter $\gamma = G/Y_0$, which controls the non-Hermiticity and phase transition of the generalized PT-symmetric electromagnetic system in Figure 1a. The transition between the exact and broken symmetry, typical for PT systems, can be characterized by the evolution of eigenvalues $\lambda_\pm$ and eigenstates $\varphi_\pm$ of $\mathbf{S}$ as a function of γ, as shown in Figure 2a; details of $\mathbf{S}$ and $\lambda_\pm$ can be found in Methods. It is seen from Figure 2a that two eigenvalues collapse into one at the EP ($\gamma = 2$), dividing the system into two distinct phases. In the exact PT-symmetry phase ($\gamma > 2$), the eigenvalues are nondegenerate and unimodular ($|\lambda_\pm| = 1$), whereas in the broken PT-symmetric phase ($\gamma < 2$), the eigenvalues are nonunimodular ($\lambda_+ = (\lambda_-^*)^{-1}$).[13] From Figure 2a, we find that in the broken symmetry phase, a self-dual spectral singularity is achieved at $\gamma = \sqrt{2}$, where the zero and infinitely large eigenvalues stand for the CPA and lasing states, respectively. The system's output can be cast into the form: $|\psi_{out}\rangle = \sum_j \lambda_j c_j |\psi_j\rangle$, where the coefficient c_j depends on the initial condition as $|\psi_{in}\rangle = \sum_j c_j|\varphi_j\rangle$. Scattering intensities at the CPAL point can be characterized by the output coefficient Θ, defined as the ratio of the total intensity of outgoing waves to that of incoming waves:

$$\Theta = \frac{|\psi_b^-|^2 + |\psi_f^+|^2}{|\psi_f^-|^2 + |\psi_b^+|^2} = \frac{|1 + \alpha M_{12}|^2 + |\alpha - M_{21}|^2}{(1 + |\alpha|^2)|M_{22}|^2} \quad (1)$$

where $\alpha = \psi_b^+/\psi_f^-$ is the ratio of complex amplitude between the two incident waves (see Methods for the explicit form of Θ). Interestingly, coherent absorption and lasing may be selectively achieved via appropriate choices of initial conditions.[37] The CPA state with $\Theta \approx 0$ can be reached when $\alpha = M_{21}$ (such a condition also makes $c_j\lambda_j \sim 0$), whereas a laser with an infinitely large output can be obtained when $\alpha \neq M_{21}$. Figure 2b presents Θ versus frequency for the PT-symmetric electromagnetic system in Figure 1a locked to the CPAL point, with $\alpha = |M_{21}|e^{i\phi}$ and $M_{21} = i(\sqrt{2} - 1)$. From Figure 2b, we find that through adjustment of the phase offset ϕ between the two incoming waves, the PT system can act either as a CPA or as a laser oscillator, resulting in a drastic change in output coefficient at the operating frequency.

CPAL-ENHANCED ELECTROMAGNETIC SENSING

Next, we study the effect of reactive perturbation on the output coefficient of the generalized PT-symmetric electromagnetic system locked to the CPAL point, as illustrated in Figure 1a. As expected, a reactive disturbance $\delta Y = i(\delta B)$, albeit very small, may abruptly switch the system from the CPA state to the laser state and vice versa; this will significantly modulate the amplitude of Θ. Considering a surface susceptance change $\mu = \delta B/Y_0 \ll 1$ and $\alpha = i(\sqrt{2} - 1)$, the output can be approximately written as (see Methods for the detailed derivation):

$$\Theta_{PT} \approx \frac{1}{4}\left[(\delta x)^2 + \frac{\mu^2}{(\delta x)^2} + O(\mu^3)\right] \quad (2)$$

Equation 2 states that sensitivity related to the slope of $\Theta_{PT}(\mu^2)$ can be boosted by an augmenting factor, $1/(\delta x)^2$, and that the output coefficient has a lower bound given by $\min(\Theta_{PT}) = (\delta x)^2/4$. Intuitively, when the phase offset δx is close to zero, an infinite slope may be obtained, thus, implying an unprecedentedly high sensitivity. Such an outcome is not feasible in traditional electromagnetic sensing systems, such as Fabry-Perot interferometers.[52] A Fabry−Perot cavity, which is formed by two positive conductances $+G$ separated by a length $x = \pi + \delta x$, can also achieve coherent perfect absorption by setting $\alpha = -1$. If a small δB is introduced to one end of a Fabry−Perot interferometer, the output coefficient can be approximately expressed as (see Methods for detailed derivation):

https://dx.doi.org/10.1021/acsphotonics.0c00514
ACS Photonics XXXX, XXX, XXX−XXX

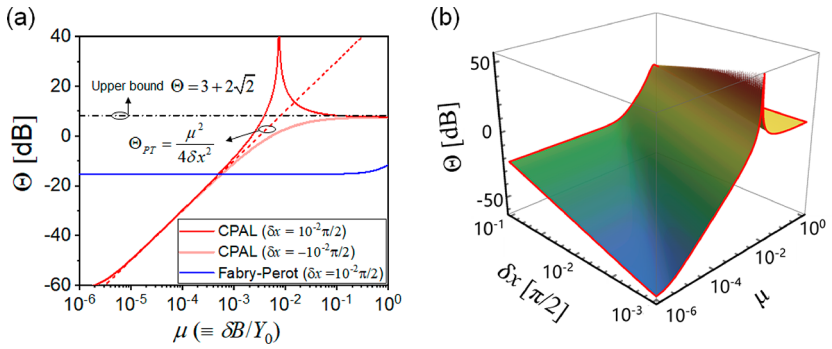

Figure 3. (a) Comparison between the CPAL-locked PT-symmetric electromagnetic sensing system in Figure 1a (red lines) and the traditional Fabry−Perot cavity sensor (blue lines) under small reactive perturbations ($\mu = \delta B/Y_0$); here, the phase shift $\delta x = 10^{-3} \times (\pi/2)$ and $c = \sqrt{2}$. Dashed lines are approximate results obtained from eqs 2 and 3. (b) Contours of output coefficient as a function of γ and δx for the CPAL-locked PT-symmetric sensing system in (a). Sensitivity, signified by the slope of $\Theta(\mu)$ in the log scale, undergoes a drastic increase as $(\delta x)^2$ decreases.

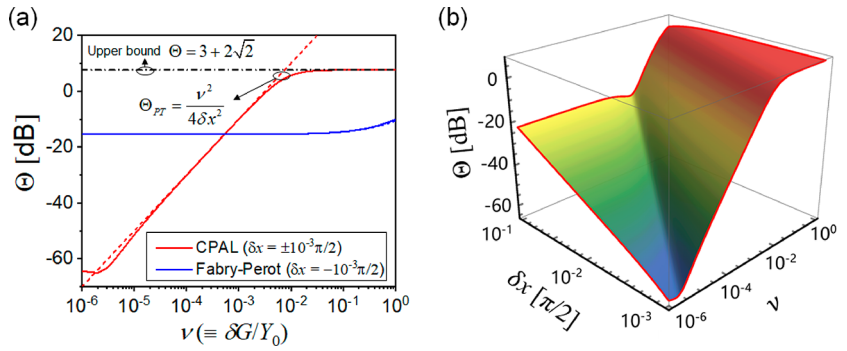

Figure 4. (a) and (b) are similar to Figures 3a and b, but for very small conductive perturbations ($\nu = \delta G/Y_0$); here $\delta x = 10^{-3} \times (\pi/2)$. Dashed lines are approximate results obtained from eqs 4 and 5. In this case, $\Theta(\nu)$ is not affected by the sign of δx. We note that sensitivity, signified by the slope of $\Theta(\nu)$ in the log scale, undergoes a drastic increase as $(\delta x)^2$ decreases.

$$\Theta_{\text{Fabry-Perot}} \approx \left(\frac{c-1}{c+1}\right)^2 + \frac{c\mu^2}{(c+1)^4} + O(\mu^3) \tag{3}$$

where $c = G/Y_0$. Equation 3 states that if $\mu \ll 1$, $\Theta_{\text{Fabry-Perot}}(\mu)$ is rather independent of δx and its slope is bounded in an interval: $0 \le c/(c+1)^4 \le 27/256$. Figure 3a compares output coefficient variations for the PT-symmetric system and its Fabry−Perot counterpart (here $c = \gamma = \sqrt{2}$ and $\delta x = \pm 10^{-3} \times (\pi/2)$). From Figure 3a, it is evident that CPAL actions, indeed, enable significantly improved sensitivity, particularly when μ is too small to be sensed by conventional techniques. Additionally, eqs 2 and 3 are quite accurate in predicting the output coefficient for small values of μ. The contours of Θ_{PT} as a function of δx and μ are shown in Figure 3b, which further reveal that sensitivity is increased by minimizing the phase offset δx. In other words, such results indicate that a monochromatic CPAL sensor may potentially provide superior sensitivity and high signal-to-noise ratio. For a relatively large μ, Θ_{PT} reaches an upper bound given by $\max(\Theta_{\text{PT}}) = 4 + 2\sqrt{2}$.

The generalized PT-symmetric electromagnetic sensing system working around the CPAL point can also be exploited for perceiving a small conductive variation δG, as illustrated in Figure 1a. Considering a small conduction change in the sensor $\nu = \delta G/Y_0 \ll 1$ and $\alpha = i(\sqrt{2} - 1)$, the output can be approximately expressed as (see Methods for detailed derivation):

$$\Theta_{\text{PT}} \approx \frac{1}{4}\left[(\delta x)^2 + \frac{\nu^2}{(\delta x)^2}\right] + O(\nu^3) \tag{4}$$

Under the same condition, the output coefficient of the Fabry−Perot structure with $\alpha = -1$ can be written as:

$$\Theta_{\text{Fabry-Perot}} \approx \left(\frac{c-1}{c+1}\right)^2 + \frac{2(c-1)}{(c+1)^3}\nu + O(\nu^2) \tag{5}$$

Again, it can be observed from eqs 4 and 5 that the CPAL-locked PT-symmetric sensing system may outperform the traditional one, as the slope of $\Theta_{\text{PT}}(\nu^2)$ can be augmented by a factor of $1/(\delta x)^2$. In contrast, the slope of the $\Theta_{\text{Febry-Perot}}$ is limited in a range, $-2 \le 2(c-1)/(c+1)^3 \le 2/27$, which shows fundamental limits on sensitivity of Fabry−Perot interferometric sensors. Figure 4a compares electromagnetic sensing systems based on the Fabry−Perot and PT-symmetric structures (here $c = \gamma = \sqrt{2}$ and $\delta x = \pm 10^{-3} \times (\pi/2)$), in response to the conductive perturbation ν. We find that significant sensitivity enhancement ascribed to the abrupt switch between CPA and lasing modes can be accomplished for conductive sensing applications. Additionally, eqs 4 and 5 are quite accurate in predicting output responses in the small-argument region. Contours of Θ_{PT} as a function of δx and ν, as shown in Figure 4b, clearly show that the sensitivity can be enhanced by reducing $(\delta x)^2$. For a relatively large ν, Θ_{PT} has upper and lower bounds given by $\max(\Theta_{\text{PT}}) = 3 + 2\sqrt{2}$ and $\min(\Theta_{\text{PT}}) = (\delta x)^2/4$. In the Supporting Information, we have briefly discussed effects of background noise on the lower

https://dx.doi.org/10.1021/acsphotonics.0c00514
ACS Photonics XXXX, XXX, XXX−XXX

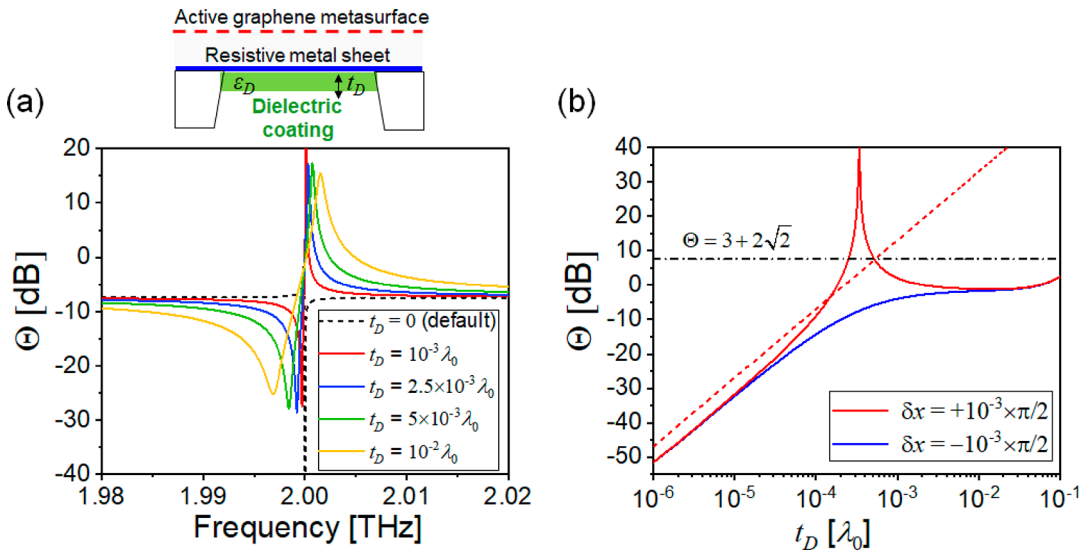

Figure 5. (a) Output coefficient variations for CPAL-locked *PT*-symmetric metasurfaces composed of an active graphene metasurface with $-G = \sqrt{2}\,Y_0$ and a passive metal filament with $G = \sqrt{2}\,Y_0$, under different levels of capacitive perturbations introduced by an ultrathin dielectric layer with thickness t_D, as shown in the inset; here, the design frequency is 2 THz. (b) Output coefficient versus the dielectric thickness for the CPAL-locked PT-symmetric sensing system in (a) (red line); here, an approximate solution given by eq 2 (red dashed line) is also shown.

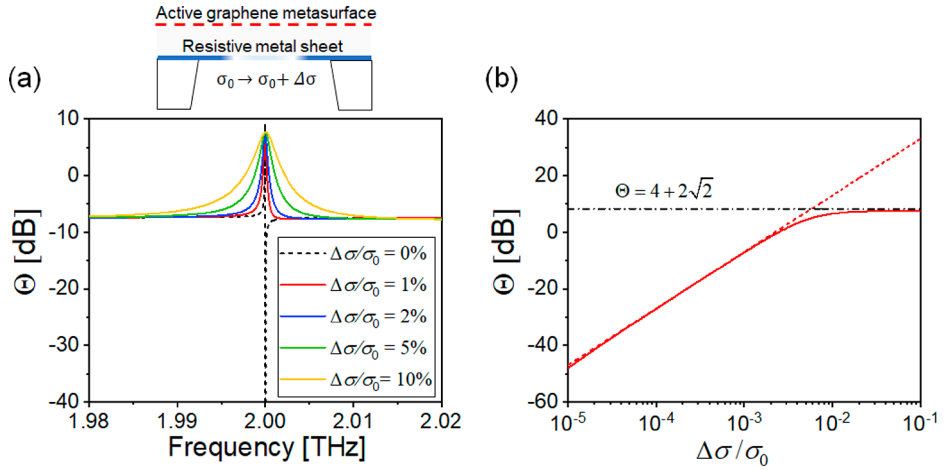

Figure 6. (a) and (b) are similar to Figure 5a and b, but for conductive perturbations introduced to the passive metasurface (when the electrical conductivity of metal σ_0 is increased by $\Delta\sigma$), as schematically shown in the inset.

bound of sensing capability for CPAL-locked PT-symmetric electromagnetic sensors. Here, the thermal (or Johnson-Nyquist) noise existing in resistive and active components is the dominant noise source, which, however, has little effect on the performance of CPAL-locked PT-symmetric electromagnetic sensors, provided that input powers are sufficiently large.

CPAL SENSING SYSTEMS BASED ON PT-SYMMETRIC METASURFACES

In the following, we will discuss practical realization of CPAL-enhanced terahertz and infrared sensors based on PT-symmetric metasurfaces. This system is composed of an active, photopumped graphene metasurface with negative surface conductance and a metallic filament with positive surface conductance ($\gamma = \sqrt{2}$); the two surfaces are separated by a suitable distance in air ($d = \lambda_0/4 \pm \Delta$ and λ_0 is the design wavelength). Population inversion may take place in a photopumped graphene metasurface due to cascaded optical photon emissions, and, further, interband transitions near the Dirac point leads to amplified spontaneous emission and optical gain in the long-wavelength region[S0,S1] (see Methods for details of active graphene metasurfaces). In the same spectral range, the sheet conductance of a metal thin film with thickness t and conductivity σ can be expressed as $G \approx \sigma t$.

We first illustrate this CPAL system by an example of dielectric sensing, of which a thin dielectric layer appearing on the passive surface (see Figure 1c) introduces a local capacitive disturbance. In the transmission line model (Figure 1a), a deep-subwavelength dielectric film can be approximately described by a lumped susceptance $\delta B/Y_0 = \mu \approx i2\pi\varepsilon_D t_D$, where ε_D and t_D are dielectric constant and thickness of the film; here $e^{i\omega t}$ time convention is adopted. Figure 5a depicts calculated spectral responses of Θ for the CPAL-locked dielectric sensing system, with a deep-subwavelength dielectric layer ($\varepsilon_D = 2.25$) adhered to the passive surface (see the inset); here, design frequency $f_0 = 2$ THz, $d = 1.001 \times (\lambda_0/4)$, and the dielectric layer is modeled as a short segment with length

https://dx.doi.org/10.1021/acsphotonics.0c00514
ACS Photonics XXXX, XXX, XXX−XXX

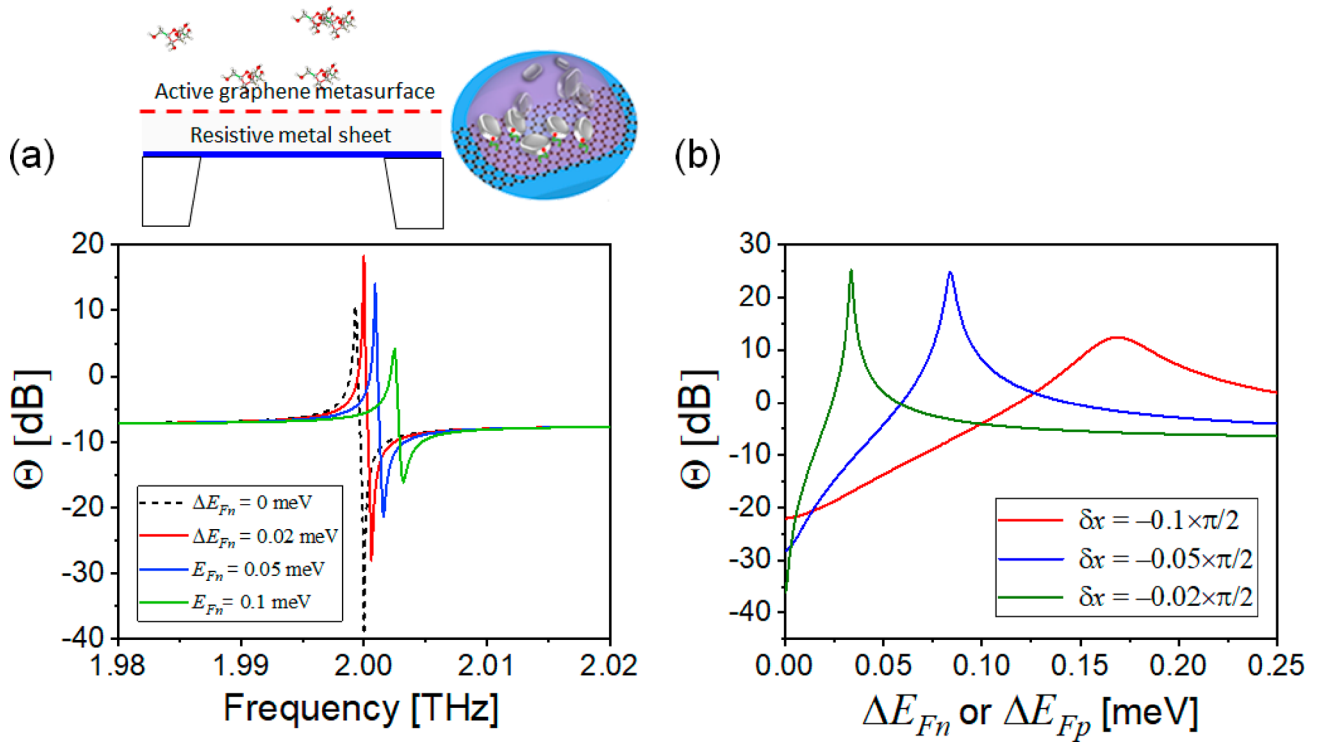

Figure 7. (a) and (b) are similar to Figure 5a and b, but for admittance perturbations occurring on the graphene surface; here, n- or p-type dopants of different densities may cause a shift in the quasi-Fermi level of graphene (ΔE_{Fn} or ΔE_{Fp}). Results in (b) show that the sensitivity can be boosted by reducing $(\delta x)^2$.

$x_D = \sqrt{\varepsilon_D}\beta_0 t_D$ and admittance $Y_D = \sqrt{\varepsilon_D} Y_0$ in the TLN model. From Figure 5a, we find that even very little change in dielectric thickness may modulate the output coefficient by several orders of magnitude. As a result, this electromagnetic sensing system may ensure detection of small-scale dielectric property changes, with ultrahigh sensitivity and resolvability. Figure 5b compares calculated Θ versus dielectric thickness for the CPAL-locked PT sensing system. It is evident that slope, as a measure of sensitivity, is nearly consistent with that predicted in eq 2, even though there is a small error due to the approximate expression of the lumped susceptance. As a result, this CPAL-locked PT-symmetric sensing system may be regarded as a promising platform for ultrasensitive dielectric sensing, which has several potential applications, including detection of gases, microliquids (aqueous solutions), aerosols, or low-density surface adsorbates that barely change the surface admittance.

Similarly, the above CPAL-locked PT-symmetric metasurfaces can be exploited to build high-performance conductive sensors, in which a conductive disturbance $\delta G/Y_0 = \nu \approx \Delta\sigma t/Y_0$ is introduced to the passive metasurface, as shown in the inset of Figure 6a. Conductive perturbations could be due to conductivity fluctuations $\Delta\sigma$ in a granular metal changes (e.g., cracks, oxidization, doping, or grain-boundary diffusion could change surface morphology and electrical properties of metals). Figure 6a presents calculated spectral responses of Θ for the CPAL-locked conductive sensing system at different values of $\Delta\sigma$. It can be seen from Figure 6a that even a very small change in conductivity can significantly modulate the output magnitude, analogous to the dielectric sensing cases in Figure 5. Figure 6b compares calculated variations of Θ with respect to the conductance change for this CPAL-based conductive sensing system. The obtained results have once again demonstrated the effectiveness of the proposed technique in detecting small-scale admittance changes, with a trend that can be well predicted using eq 4.

Last, but not least, graphene monolayer/bilayer metasurfaces have been reported to exhibit a chemically tunable surface admittance, which may be exploited to modulate light scattering and the output coefficient of PT-symmetric metasurfaces.[53−55] In this case, an active graphene metasurface can simultaneously provide gain and sensing function in a PT-symmetric electromagnetic sensing system, such that Θ can be instantaneously tuned due to increased amounts of n- or p-type surface adsorbates (e.g., reactive gas or ionized molecules) that alter the negative dynamic conductivity of graphene. Here, we assume that a pristine graphene is optically pumped to exhibit electron and hole quasi-Fermi levels of the same absolute value (i.e., $E_{Fn} = -E_{Fp} = 15$ meV), and n-type surface dopants further cause a small increase in electron quasi-Fermi level ΔE_{Fn}. Figure 7a depicts the calculated Θ versus frequency for the CPAL-locked PT-symmetric sensing system based on a photopumped graphene metasurface at different doping levels; here $d = \lambda_0/4.05$. These results show that a large modulation depth (>60 dB) may be obtained due to an meV-scale change in graphene's quasi-Fermi level. We note that both n-type and p-type shifts lead to the same perturbation in the effective surface admittance of graphene metasurface, since graphene has a linear energy-momentum dispersion near the Dirac point. Figure 7b plots the magnitude of output coefficient versus the ΔE_{Fn} (or ΔE_{Fp}) at the CPAL frequency. It can be seen that slight n- or p-doping in graphene may break the coherence of the two incident waves and therefore switch the system from the CPA state to the lasing state in a rapid and almost binary-like manner. Such an effect leads to an ultrahigh sensitivity, well beyond passive graphene-metasurface sensors.[54] It is

https://dx.doi.org/10.1021/acsphotonics.0c00514
ACS Photonics XXXX, XXX, XXX−XXX

worth mentioning that since graphene is made of a single layer of carbon atoms, further surface functionalization may guarantee good selectivity for chemical, molecular, and biological sensing.

CONCLUSIONS

We have shown that a PT-symmetric CPA-laser, when loaded with a variable-admittance element, may be exploited to realize monochromatic electromagnetic sensing systems with unprecedented sensitivity. Around the CPAL point of the system, a small-scale conductive or reactive disturbance may lead to a drastic change in the output-to-input ratio. Moreover, we have theoretically proven that the sensitivity, expressed as the slope of the output coefficient relative to the change in admittance, can be tailored at will by a phase-related augmenting factor. Different from EP-based sensors,[20−23,31,47,48] the proposed CPAL-locked sensing paradigm does not rely on frequency-swept measurements (i.e., tracking the resonance frequency drift enhanced by the eigenvalue bifurcation) and, thus, may avoid the phase noise, flicker noise, modal interreference, and limited spectrum shortage. We have also illustrated practical implementation of a CPAL-locked optical sensing system using PT-symmetric metasurfaces in conjunction with a variable shunt admittance. Our results unveil exciting possibilities for building the next-generation ultrasensitive electromagnetic sensors in different spectral ranges.

METHODS

Scattering and Transfer Matrices. The scattering matrix **S** of the PT-symmetric system in Figure 1a can be derived as

$$|\psi_{out}\rangle = \mathbf{S}|\psi_{in}\rangle;$$

$$\mathbf{S} = \begin{pmatrix} t & r^{+} \\ r^{-} & t \end{pmatrix} = \begin{pmatrix} \dfrac{1}{e^{ix} - i\gamma^2\sin(x)/2} & \dfrac{(1+2/\gamma)\sin(x)}{-\sin(x) - 2ie^{ix}/\gamma^2} \\ \dfrac{(1-2/\gamma)\sin(x)}{-\sin(x) - 2ie^{ix}/\gamma^2} & \dfrac{1}{e^{ix} - i\gamma^2\sin(x)/2} \end{pmatrix} \tag{6}$$

The transition between the exact and broken symmetry can be known from tracing the evolution of eigenvalues of **S**, given by

$$\lambda_{\pm} = \frac{2/\gamma^2 \pm \sqrt{(4/\gamma^2 - 1)\sin^2(x)}}{2e^{ix}/\gamma^2 - i\sin(x)} \tag{7}$$

In physical systems, an optical laser or an RF/microwave oscillator generates output without any ac input signal (i.e., $|\psi_{out}\rangle \neq 0$, whereas $|\psi_{in}\rangle \sim 0$), which implies $M_{22} = 0$. In the reverse scenario, although $|\psi_{in}\rangle \neq 0$, a CPA can lead to $|\psi_{out}\rangle = 0$, which implies $M_{11} = 0$. Since the PT system is reciprocal (i.e., $\det(\mathbf{M}) = 1$) and requires that $\mathbf{M}^* = \mathbf{M}^{-1}$, an exotic property, $M_{11} = M_{22} = 0$, occurs at the CPAL point. The system can operate in the CPA state if $\alpha = M_{21}$, whereas it can be readily switched to the lasing state if $\alpha \neq M_{21}$.

Expressions for Output Coefficients. When a reactive perturbation $\mu = \delta B/Y_0$ is introduced to the loss or gain side of the PT-symmetric electromagnetic system locked to the CPAL point ($\gamma = \sqrt{2}$, $x = \pi/2 + \delta x$ and $\alpha = M_{21} = i(\sqrt{2} - 1)$), the output coefficient can be written as

$$\Theta_{PT} = \frac{4 - \sec(\delta x)(8 - (\mu^2 + 4)\sec(\delta x))}{(2\sqrt{2} - 3)\mu^2 - 4(\sqrt{2} - 1)\mu\tan(\delta x) + (\mu^2 + 4)\tan^2(\delta x)}$$
$$\approx \frac{\mu^2}{4(\delta x)^2} + O(\mu^3), \quad \text{if } \mu \ll 1 \tag{8}$$

With the same amount of μ, the output coefficient for a Fabry−Perot CPA with $\alpha = -1$ can be derived as

$$\Theta_{\text{Fabry-Perot}} = \frac{\begin{bmatrix} c^4 + (c^2+1)\delta^2 + (4c^2 + \delta^2)\cot^2(\delta x) \\ + 4\csc(\delta x)(c\delta + \csc(\delta x)) \\ - 2c\ \cot(\delta x)(c\delta + 4\csc(\delta x)) \end{bmatrix}}{\begin{bmatrix} (c^2 + 2c + 2)^2 + \delta^2(c+1)^2 - 2(c^2 + 2c)\delta\ \cot(\delta x) \\ + (4(c+1)^2 + \delta^2)\cot^2(\delta x) \end{bmatrix}}$$
$$\approx \left(\frac{c-1}{c+1}\right)^2 + \frac{c\mu^2}{(c+1)^4} + \frac{2c\mu}{(c+1)^4}\delta x + O(\mu^3), \quad \text{if } \mu \ll 1$$
$$\approx \left(\frac{c-1}{c+1}\right)^2 + \frac{c\mu^2}{(c+1)^4} \tag{9}$$

Similarly, when a conductive perturbation $\nu = \delta G/Y_0$ is introduced to the loss side of CPAL-locked PT-symmetric electromagnetic system with $\alpha = M_{21} = i(\sqrt{2} - 1)$, the output coefficient can be written as

$$\Theta_{PT} = \frac{2\sqrt{2}\nu(\sec(\delta x) - 1) - 4(\sec(\delta x) - 1)^2 - \nu^2\sec^2(\delta x)}{(2\sqrt{2} - 3)\nu^2 - (\nu + 2)^2\tan^2(\delta x)}$$
$$\approx \frac{1}{4}\left[(\delta x)^2 + \frac{\nu^2}{(\delta x)^2} - \frac{(8 - 3\sqrt{2})}{4}\frac{\nu^3}{(\delta x)^2} + O(\nu^4)\right], \quad \text{if } \nu \ll 1$$
$$\approx \frac{1}{4}\frac{\nu^2}{(\delta x)^2} \tag{10}$$

If a Fabry−Perot CPA with $\alpha = -1$ is considered, the output coefficient can be derived as

$$\Theta_{\text{Fabry-Perot}} = \frac{c^3(c+2\nu) + (c^2+1)\nu^2 + [(2c+\nu)\cot(\delta x) - 2\csc(\delta x)]^2}{[(c+1)(\nu+2) + c^2]^2 + [2(c+1) + \nu]^2\cot^2(\delta x)}$$
$$\approx \left(\frac{2(c-1) + \nu}{2(c+1) + \nu}\right)^2, \quad \text{if } \nu \ll 1$$
$$\approx \frac{(c-1)^2}{(c+1)^2} + \frac{2(c-1)}{(c+1)^3}\nu^2 \tag{11}$$

Active, Optically Pumped Graphene Metasurface. The nonequilibrium (dynamic) conductivity of graphene taking into account both interband and intraband transitions $\sigma = \sigma_{intra} + \sigma_{inter}$ can be written as

$$\sigma_{intra} = i\frac{q^2}{\pi\hbar^2}\frac{1}{\omega - i\tau^{-1}}\left[\int_0^{\infty}\varepsilon\left(\frac{\partial F_1(\varepsilon)}{\partial\varepsilon} - \frac{\partial F_2(-\varepsilon)}{\partial\varepsilon}\right)d\varepsilon\right] \tag{12a}$$

$$\sigma_{inter} = -i\frac{q^2}{\pi\hbar^2}(\omega - i\tau^{-1})\int_0^{\infty}\frac{F_2(-\varepsilon) - F_1(\varepsilon)}{(\omega - i\tau^{-1})^2 - 4\varepsilon^2/\hbar^2}d\varepsilon \tag{12b}$$

where $F_1(\varepsilon) = [1 + e^{(\varepsilon - E_{Fn})/K_BT}]^{-1}$, $F_2(\varepsilon) = [1 + e^{(\varepsilon - E_{Fp})/K_BT}]^{-1}$, q is the electric charge, ε is the energy, $\hbar$ is the reduced Planck's constant, K_B is the Boltzmann's constant, T is the temperature (here, we assume $T = 77$ K), ω is the angular frequency, and τ is the momentum relaxation time of charge carriers (here, we

https://dx.doi.org/10.1021/acsphotonics.0c00514
ACS Photonics XXXX, XXX, XXX−XXX

assume τ = 1 ps, which agrees with experimental results). The interband transitions and the cascaded optical-phonon emission may lead to photoexcited electron-hole pairs near the Dirac point, splitting the Fermi level into electron and hole quasi-Fermi levels (i.e., E_{Fn}, $E_{Fp} = \pm\varepsilon_F$ in eq 12). In this case, Re[σ_{inter}] in eq 12b may be negative, which, however, must compete with the positive Re[σ_{intra}] in eq 12a.

According to impedance boundary conditions, a discontinuity of the tangential magnetic field on the metasurface can be related to the induced averaged surface current by the surface admittance Y_s. Assuming an array of perfectly conducting strips of negligible thickness (see Figure 1c) are aligned parallel to the magnetic field of the transverse magnetic (TM) incident wave, the equivalent surface admittance can be explicitly written as[47,48]

$$Y_s = -i2\alpha Y_{eff},$$

$$\text{and } \xi = \frac{\beta_{eff}p}{\pi}\left[\ln\left(\csc\left(\frac{\pi g}{2p}\right)\right) + \frac{1}{2}\sum_{n=-\infty,n\neq 0}^{\infty}\left(\frac{2\pi}{\sqrt{(2\pi n)^2 - \beta_{eff}^2 p^2}} - \frac{1}{|n|}\right)\right]$$

$$\approx \frac{\beta_{eff}p}{\pi}\ln\left(\csc\left(\frac{\pi g}{2p}\right)\right) \text{ if } \beta_{eff}p \ll 2\pi \tag{13}$$

where g and p are the gap width and period of the strip array, $Y_{eff} = \sqrt{\varepsilon_{eff}/\mu_0}$, $\beta_{eff} = \omega\sqrt{\mu_0\varepsilon_{eff}}$, $\varepsilon_{eff} = (\varepsilon + \varepsilon_0)/2$, ε_0 and ε are permittivities of air and the host substrate, respectively. When a dispersive medium such as graphene is used to constitute the metasurface, the surface admittance is usually complex-valued, and its real (surface conductance) and imaginary parts (surface susceptance) account for the gain/loss magnitude and the net stored energy in the near field, respectively. When considering a complex-valued sheet conductivity, the surface impedance of the metasurface should be modified as[48]

$$Y_s = \left[\frac{1}{\sigma_s(1 - g/p)} - i\frac{1}{2\xi Y_{eff}}\right]^{-1} \tag{14}$$

By tailoring the geometric parameters, g and p, it is possible that the kinetic inductance of a plasmonic material can cancel out the imaginary part of the geometric (surface) capacitance, so as to achieve a purely real, positive, or negative surface admittance at the frequency of interest. In Figures 5, 6, and 7, we used a graphene metasurface with ε_F = 15 meV, p = 2.211 μm, and g = 0.332 μm, which yield a surface admittance ε_F = 15 meV at the design frequency (f_0 = 2 THz).

■ ASSOCIATED CONTENT

Supporting Information

The Supporting Information is available free of charge at https://pubs.acs.org/doi/10.1021/acsphotonics.0c00514.

Additional experimental and computational details (PDF)

■ AUTHOR INFORMATION

Corresponding Author

Pai-Yen Chen − *Department of Electrical and Computer Engineering, University of Illinois at Chicago, Chicago, Illinois 60607, United States*; Email: pychen@uic.edu

Authors

Mohamed Farhat − *Computer, Electrical, and Mathematical Science and Engineering Division, King Abdullah University of Science and Technology, Thuwal 23955, Saudi Arabia*; orcid.org/0000-0003-0351-4309

Minye Yang − *Department of Electrical and Computer Engineering, University of Illinois at Chicago, Chicago, Illinois 60607, United States*

Zhilu Ye − *Department of Electrical and Computer Engineering, University of Illinois at Chicago, Chicago, Illinois 60607, United States*

Complete contact information is available at: https://pubs.acs.org/10.1021/acsphotonics.0c00514

Notes

The authors declare no competing financial interest.

■ ACKNOWLEDGMENTS

This work was supported by the NSF ECCS-1917678 Grant.

■ REFERENCES

(1) El-Ganainy, R.; Makris, K. G.; Christodoulides, D. N.; Musslimani, Z. H. Theory of Coupled Optical PT-Symmetric Structures. *Opt. Lett.* **2007**, *32* (17), 2632.

(2) El-Ganainy, R.; Makris, K. G.; Khajavikhan, M.; Musslimani, Z. H.; Rotter, S.; Christodoulides, D. N. Non-Hermitian Physics and PT Symmetry. *Nat. Phys.* **2018**, *14* (1), 11−19.

(3) Guo, A.; Salamo, G. J.; Duchesne, D.; Morandotti, R.; Volatier-Ravat, M.; Aimez, V.; Siviloglou, G. A.; Christodoulides, D. N. Observation of P T -Symmetry Breaking in Complex Optical Potentials. *Phys. Rev. Lett.* **2009**, *103* (9), 093902.

(4) Ramezani, H.; Kottos, T.; El-Ganainy, R.; Christodoulides, D. N. Unidirectional Nonlinear PT -Symmetric Optical Structures. *Phys. Rev. A: At., Mol., Opt. Phys.* **2010**, *82* (4), 043803.

(5) Lin, Z.; Ramezani, H.; Eichelkraut, T.; Kottos, T.; Cao, H.; Christodoulides, D. N. Unidirectional Invisibility Induced by P T -Symmetric Periodic Structures. *Phys. Rev. Lett.* **2011**, *106* (21), 213901.

(6) Feng, L.; Xu, Y.-L.; Fegadolli, W. S.; Lu, M.-H.; Oliveira, J. E. B.; Almeida, V. R.; Chen, Y.-F.; Scherer, A. Experimental Demonstration of a Unidirectional Reflectionless Parity-Time Metamaterial at Optical Frequencies. *Nat. Mater.* **2013**, *12* (2), 108−113.

(7) Doppler, J.; Mailybaev, A. A.; Böhm, J.; Kuhl, U.; Girschik, A.; Libisch, F.; Milburn, T. J.; Rabl, P.; Moiseyev, N.; Rotter, S. Dynamically Encircling an Exceptional Point for Asymmetric Mode Switching. *Nature* **2016**, *537* (7618), 76−79.

(8) Rechtsman, M. C. Optical Sensing Gets Exceptional. *Nature* **2017**, *548* (7666), 161−162.

(9) Miri, M.-A.; Alù, A. Exceptional Points in Optics and Photonics. *Science* **2019**, *363* (6422), No. eaar7709.

(10) Özdemir, Ş. K.; Rotter, S.; Nori, F.; Yang, L. Parity-Time Symmetry and Exceptional Points in Photonics. *Nat. Mater.* **2019**, *18* (8), 783−798.

(11) Savoia, S.; Castaldi, G.; Galdi, V.; Alù, A.; Engheta, N. Tunneling of Obliquely Incident Waves through PT -Symmetric Epsilon-near-Zero Bilayers. *Phys. Rev. B: Condens. Matter Mater. Phys.* **2014**, *89* (8), 085105.

(12) Savoia, S.; Castaldi, G.; Galdi, V. Non-Hermiticity-Induced Wave Confinement and Guiding in Loss-Gain-Loss Three-Layer Systems. *Phys. Rev. A: At., Mol., Opt. Phys.* **2016**, *94* (4), 043838.

(13) Chong, Y. D.; Ge, L.; Stone, A. D. P T -Symmetry Breaking and Laser-Absorber Modes in Optical Scattering Systems. *Phys. Rev. Lett.* **2011**, *106* (9), 093902.

(14) Zhu, X.; Ramezani, H.; Shi, C.; Zhu, J.; Zhang, X. P T -Symmetric Acoustics. *Phys. Rev. X* **2014**, *4* (3), 031042.

(15) Fleury, R.; Sounas, D.; Alù, A. An Invisible Acoustic Sensor Based on Parity-Time Symmetry. *Nat. Commun.* **2015**, *6* (1), 5905.
(16) Schindler, J.; Li, A.; Zheng, M. C.; Ellis, F. M.; Kottos, T. Experimental Study of Active *LRC* Circuits with PT Symmetries. *Phys. Rev. A: At., Mol., Opt. Phys.* **2011**, *84* (4), 040101.
(17) Schindler, J.; Lin, Z.; Lee, J. M.; Ramezani, H.; Ellis, F. M.; Kottos, T. \textdollar\textbackslashmathcal$\lbrace$PT$\rbrace$ \textdollar-Symmetric Electronics. *J. Phys. A: Math. Theor.* **2012**, *45* (44), 444029.
(18) Lee, J. M.; Factor, S.; Lin, Z.; Vitebskiy, I.; Ellis, F. M.; Kottos, T. Reconfigurable Directional Lasing Modes in Cavities with Generalized P T̃ Symmetry. *Phys. Rev. Lett.* **2014**, *112* (25), 253902.
(19) Ra'di, Y.; Sounas, D. L.; Alù, A.; Tretyakov, S. A. Parity-Time-Symmetric Teleportation. *Phys. Rev. B: Condens. Matter Mater. Phys.* **2016**, *93* (23), 235427.
(20) Chen, P.-Y.; Sakhdari, M.; Hajizadegan, M.; Cui, Q.; Cheng, M. M.-C.; El-Ganainy, R.; Alù, A. Generalized Parity-Time Symmetry Condition for Enhanced Sensor Telemetry. *Nat. Electron* **2018**, *1* (5), 297−304.
(21) Sakhdari, M.; Hajizadegan, M.; Li, Y.; Cheng, M. M.-C.; Hung, J. C. H.; Chen, P.-Y. Ultrasensitive, Parity-Time-Symmetric Wireless Reactive and Resistive Sensors. *IEEE Sens. J.* **2018**, *18* (23), 9548−9555.
(22) Sakhdari, M.; Hajizadegan, M.; Zhong, Q.; Christodoulides, D. N.; El-Ganainy, R.; Chen, P.-Y. Experimental Observation of P T Symmetry Breaking near Divergent Exceptional Points. *Phys. Rev. Lett.* **2019**, *123* (19), 193901.
(23) Dong, Z.; Li, Z.; Yang, F.; Qiu, C.-W.; Ho, J. S. Sensitive Readout of Implantable Microsensors Using a Wireless System Locked to an Exceptional Point. *Nat. Electron* **2019**, *2* (8), 335−342.
(24) Assawaworrarit, S.; Yu, X.; Fan, S. Robust Wireless Power Transfer Using a Nonlinear Parity-Time-Symmetric Circuit. *Nature* **2017**, *546* (7658), 387−390.
(25) Sakhdari, M.; Hajizadegan, M.; Chen, P.-Y. Robust Extended-Range Wireless Power Transfer Using a Higher-Order PT-Symmetric Platform. *Phys. Rev. Research* **2020**, *2* (1), 013152.
(26) Sounas, D. L.; Fleury, R.; Alù, A. Unidirectional Cloaking Based on Metasurfaces with Balanced Loss and Gain. *Phys. Rev. Appl.* **2015**, *4* (1), 014005.
(27) Fleury, R.; Sounas, D. L.; Alù, A. Negative Refraction and Planar Focusing Based on Parity-Time Symmetric Metasurfaces. *Phys. Rev. Lett.* **2014**, *113* (2), 023903.
(28) Lin, X.; Yang, Y.; Rivera, N.; López, J. J.; Shen, Y.; Kaminer, I.; Chen, H.; Zhang, B.; Joannopoulos, J. D.; Soljačić, M. All-Angle Negative Refraction of Highly Squeezed Plasmon and Phonon Polaritons in Graphene-Boron Nitride Heterostructures. *Proc. Natl. Acad. Sci. U. S. A.* **2017**, 201701830.
(29) Peng, B.; Ozdemir, K.; Rotter, S.; Yilmaz, H.; Liertzer, M.; Monifi, F.; Bender, C. M.; Nori, F.; Yang, L. Loss-Induced Suppression and Revival of Lasing. *Science* **2014**, *346* (6207), 328−332.
(30) Chang, L.; Jiang, X.; Hua, S.; Yang, C.; Wen, J.; Jiang, L.; Li, G.; Wang, G.; Xiao, M. Parity-Time Symmetry and Variable Optical Isolation in Active-Passive-Coupled Microresonators. *Nat. Photonics* **2014**, *8* (7), 524−529.
(31) Hodaei, H.; Hassan, A. U.; Wittek, S.; Garcia-Gracia, H.; El-Ganainy, R.; Christodoulides, D. N.; Khajavikhan, M. Enhanced Sensitivity at Higher-Order Exceptional Points. *Nature* **2017**, *548* (7666), 187−191.
(32) Chen, W.; Kaya Özdemir, Ş.; Zhao, G.; Wiersig, J.; Yang, L. Exceptional Points Enhance Sensing in an Optical Microcavity. *Nature* **2017**, *548* (7666), 192−196.
(33) Chen, P.-Y.; Jung, J. P T Symmetry and Singularity-Enhanced Sensing Based on Photoexcited Graphene Metasurfaces. *Phys. Rev. Appl.* **2016**, *5* (6), 064018.
(34) Wiersig, J. Sensors Operating at Exceptional Points: General Theory. *Phys. Rev. A: At., Mol., Opt. Phys.* **2016**, *93* (3), 033809.
(35) Zhang, M.; Sweeney, W.; Hsu, C. W.; Yang, L.; Stone, A. D.; Jiang, L. Quantum Noise Theory of Exceptional Point Amplifying Sensors. *Phys. Rev. Lett.* **2019**, *123* (18), 180501.
(36) Xiao, Z.; Li, H.; Kottos, T.; Alù, A. Enhanced Sensing and Nondegraded Thermal Noise Performance Based on P T -Symmetric Electronic Circuits with a Sixth-Order Exceptional Point. *Phys. Rev. Lett.* **2019**, *123* (21), 213901.
(37) Wolff, C.; Tserkezis, C.; Mortensen, N. A. On the Time Evolution at a Fluctuating Exceptional Point. *Nanophotonics* **2019**, *8* (8), 1319−1326.
(38) Langbein, W. No Exceptional Precision of Exceptional-Point Sensors. *Phys. Rev. A: At., Mol., Opt. Phys.* **2018**, *98* (2), 023805.
(39) Mortensen, N. A.; Gonçalves, P. A. D.; Khajavikhan, M.; Christodoulides, D. N.; Tserkezis, C.; Wolff, C. Fluctuations and Noise-Limited Sensing near the Exceptional Point of Parity-Time-Symmetric Resonator Systems. *Optica* **2018**, *5* (10), 1342.
(40) Hayenga, W. E.; Parto, M.; Ren, J.; Wu, F. O.; Hokmabadi, M. P.; Wolff, C.; El-Ganainy, R.; Mortensen, N. A.; Christodoulides, D. N.; Khajavikhan, M. Direct Generation of Tunable Orbital Angular Momentum Beams in Microring Lasers with Broadband Exceptional Points. *ACS Photonics* **2019**, *6* (8), 1895−1901.
(41) Longhi, S. PT -Symmetric Laser Absorber. *Phys. Rev. A: At., Mol., Opt. Phys.* **2010**, *82* (3), 031801.
(42) Sun, Y.; Tan, W.; Li, H.; Li, J.; Chen, H. Experimental Demonstration of a Coherent Perfect Absorber with PT Phase Transition. *Phys. Rev. Lett.* **2014**, *112* (14), 143903.
(43) Wong, Z. J.; Xu, Y.-L.; Kim, J.; O'Brien, K.; Wang, Y.; Feng, L.; Zhang, X. Lasing and Anti-Lasing in a Single Cavity. *Nat. Photonics* **2016**, *10* (12), 796−801.
(44) Feng, L.; Wong, Z. J.; Ma, R.-M.; Wang, Y.; Zhang, X. Single-Mode Laser by Parity-Time Symmetry Breaking. *Science* **2014**, *346* (6212), 972−975.
(45) Hodaei, H.; Miri, M.-A.; Heinrich, M.; Christodoulides, D. N.; Khajavikhan, M. Parity-Time-Symmetric Microring Lasers. *Science* **2014**, *346* (6212), 975−978.
(46) Sakhdari, M.; Estakhri, N. M.; Bagci, H.; Chen, P.-Y. Low-Threshold Lasing and Coherent Perfect Absorption in Generalized P T -Symmetric Optical Structures. *Phys. Rev. Appl.* **2018**, *10* (2), 024030.
(47) Chen, P.-Y.; Jung, J. P T Symmetry and Singularity-Enhanced Sensing Based on Photoexcited Graphene Metasurfaces. *Phys. Rev. Appl.* **2016**, *5* (6), 064018.
(48) Wiersig, J. Sensors Operating at Exceptional Points: General Theory. *Phys. Rev. A: At., Mol., Opt. Phys.* **2016**, *93* (3), 033809.
(49) Sun, Y.; Edwards, B.; Alù, A.; Engheta, N. Experimental Realization of Optical Lumped Nanocircuits at Infrared Wavelengths. *Nat. Mater.* **2012**, *11* (3), 208−212.
(50) Watanabe, T.; Fukushima, T.; Yabe, Y.; Tombet, S. A. B.; Satou, A.; Dubinov, A. A.; Aleshkin, V. Y.; Mitin, V.; Ryzhii, V.; Otsuji, T. The Gain Enhancement Effect of Surface Plasmon Polaritons on Terahertz Stimulated Emission in Optically Pumped Monolayer Graphene. *New J. Phys.* **2013**, *15* (7), 075003.
(51) Low, T.; Chen, P.-Y.; Basov, D. N. Superluminal Plasmons with Resonant Gain in Population Inverted Bilayer Graphene. *Phys. Rev. B: Condens. Matter Mater. Phys.* **2018**, *98* (4), 041403.
(52) Vaughan, M. *The Fabry-Perot Interferometer: History, Theory, Practice and Applications*; Routledge, 2017.
(53) Chen, P.-Y.; Alu, A. Terahertz Metamaterial Devices Based on Graphene Nanostructures. *IEEE Trans. Terahertz Sci. Technol.* **2013**, *3* (6), 748−756.
(54) Rodrigo, D.; Limaj, O.; Janner, D.; Etezadi, D.; Garcia de Abajo, F. J.; Pruneri, V.; Altug, H. Mid-Infrared Plasmonic Biosensing with Graphene. *Science* **2015**, *349* (6244), 165−168.
(55) Chen, P. Y.; Farhat, M.; Bağcı, H. Graphene Metascreen for Designing Compact Infrared Absorbers with Enhanced Bandwidth. *Nanotechnology* **2015**, *26* (16), 164002.

https://dx.doi.org/10.1021/acsphotonics.0c00514
ACS Photonics XXXX, XXX, XXX−XXX